



A novel nanomedicine integrating ferroptosis and photothermal therapy, well-suitable for PD-L1-mediated immune checkpoint blockade

Yujun Bao^{a,b}, Guanghao Li^b, Siqi Li^b, Haishui Zhou^a, Ziqing Yang^c, Zhiqiang Wang^b, Rui Yan^{b,*}, Changhong Guo^{a,**}, Yingxue Jin^{a,b,***}

^a Key Laboratory of Molecular Cytogenetics and Genetic Breeding of Heilongjiang Province, College of Life Science and Technology, Harbin Normal University, Harbin, 150025, China

^b Key Laboratory for Photonic and Electronic Bandgap Materials, Ministry of Education, College of Chemistry & Chemical Engineering, Harbin Normal University, Harbin, 150025, China

^c School of Basic Medical Sciences, Shandong University, Jinan, 250012, China

ARTICLE INFO

Keywords:

Immune checkpoint blockade
Ferroptosis
Photothermal therapy
Antitumor
PD-L1

ABSTRACT

Immunotherapy based on immune checkpoint blockade has emerged as a promising treatment strategy; however, the therapeutic efficacy is limited by the immunosuppressive microenvironment. Here, we developed a novel immune-activated nanoparticle (Fc-SS-Fe/Cu) to address the issue of insufficient immune infiltration. Specifically, the structure of Fc-SS-Fe/Cu collapsed in response to the tumor microenvironment, the ferrocene and disulfide bonds and the released Fe/Cu ions can effectively generate ·OH and deplete GSH to increase oxidative stress, thereby inducing ferroptosis. Withal, the positive feedback mechanisms of "laser-triggered mild-temperature photothermal therapy (PTT), PTT accelerated ferroptosis and LPO accumulation, LPO mediated HSPs down-regulated to promote PTT," effectively triggers immunogenic cell death (ICD) in tumor cells, significantly enhancing their immunogenicity. Moreover, the O₂-generating ability induced by Fc-SS-Fe/Cu could reverse the hypoxic tumor microenvironment, and importantly, the expression of PD-L1 on tumor cell surfaces could be effectively downregulated by inhibiting the HIF-1 α pathways, thereby augmenting the effect of anti-PD-L1 (α PD-L1) therapy. Therefore, this study provides valuable strategies into enhancing PD-L1-mediated ICB therapy.

1. Introduction

Immune checkpoint blockade (ICB) therapy exhibits substantial potential in the treatment of tumor metastasis and recurrence. However, clinical research findings indicate that the efficacy of immunotherapy falls significantly short of the anticipated target due to the tumor immunosuppressive microenvironment (TIME) [1,2]. Currently, inducing immunogenic cell death (ICD) to enhance immunogenicity has emerged as an affirmed and crucial strategy for PD-L1-mediated ICB [3,4]. In the process of immune activation, activated T cells generate interferon- γ (IFN- γ). As a key mediator of the immune system, IFN- γ is capable of activating and modulating the functions of various immune cells. It can promote the proliferation, activation, and differentiation of immune cells and enhance the killing ability of immune cells against

tumor cells [5,6]. However, it should be noted that IFN- γ also regulates the expression of PD-L1 on the surface of tumor cells simultaneously, which may be not conducive to the effect of ICB [7,8]. Hence, relatively downregulating PD-L1 expression will be another valuable and effective strategy to enhance the efficacy of PD-L1-mediated ICB. The Warburg effect exhibited by tumor cells leads to their unique energy acquisition mechanism and metabolic abnormalities, resulting in a weakly acidic and hypoxic environment that effectively hampers the metabolic activity of CD8⁺ T cells while promoting various immunosuppressive cell functions [9,10]. Importantly, the hypoxia-induced upregulation of HIF-1 α can effectively stimulate the expression of PD-L1 [11,12], which is an overlooked yet crucial pathway to regulate the expression of PD-L1. Therefore, augmenting immunogenicity *via* ICD in conjunction with downregulating PD-L1 by reversing hypoxia will be a novel approach to

* Corresponding author.

** Corresponding author.

*** Corresponding author.

E-mail addresses: yanrui-1981@163.com (R. Yan), guoprof@163.com (C. Guo), jyxprof@163.com (Y. Jin).

<https://doi.org/10.1016/j.mtbio.2024.101346>

Received 18 August 2024; Received in revised form 3 November 2024; Accepted 15 November 2024

Available online 16 November 2024

2590-0064/© 2024 The Authors. Published by Elsevier Ltd. This is an open access article under the CC BY-NC-ND license (<http://creativecommons.org/licenses/by-nc-nd/4.0/>).

augment the efficacy of PD-L1-mediated ICB therapy.

Ferroptosis, characterized by the accumulation of lipid peroxides (LPO), has emerged as a potential strategy for reversing immune suppression in the tumor microenvironment in cancer therapy [13,14]. Due to the metabolic abnormalities of tumor cells, they exhibit a heightened dependence on antioxidant mechanisms, rendering them more susceptible to oxidative stress [15,16]. Consequently, the most direct approach involves inducing lipid peroxidation by enhancing oxidative stress through the generation of hydroxyl radicals ($\cdot\text{OH}$) via Fenton/Fenton-like reactions facilitated by transition metal ions such as Fe^{2+} and Cu^+ [17–19]. Furthermore, the generation of O_2 during the Fenton/Fenton-like reaction process can effectively address tumor hypoxia, which is anticipated to downregulate HIF-1 α and PD-L1 expression while increasing T cell infiltration. Currently, mild-temperature photothermal therapy (PTT) ($\leq 50^\circ\text{C}$) represents a promising treatment modality in the field of optical tumor therapy, as it effectively circumvents the detrimental thermal damage ($>50^\circ\text{C}$) to adjacent healthy tissues [20–22]. However, its efficacy is constrained by the presence of heat shock proteins (HSPs) [23–25]. The existence of studies demonstrates that accumulated LPO has the potential to eliminate excessive HSPs mediated by PTT. The main mechanisms are likely as follows: Excessive LPO can cause an imbalance in the intracellular redox state, disrupting the structure and function of HSPs and making it more susceptible to degradation. Alternatively, LPO may activate specific signaling pathways and prompt cells to initiate the clearance mechanism for excessive HSPs, thereby augmenting the therapeutic effects of PTT [26,27]. Additionally, PTT can also enhance ferroptosis through the Fenton/Fenton-like reaction [28–30]. Therefore, the rational development of integrated nanomedicines combining ferroptosis/PTT/oxygen generation for immunotherapy represents a promising and underexplored therapeutic strategy.

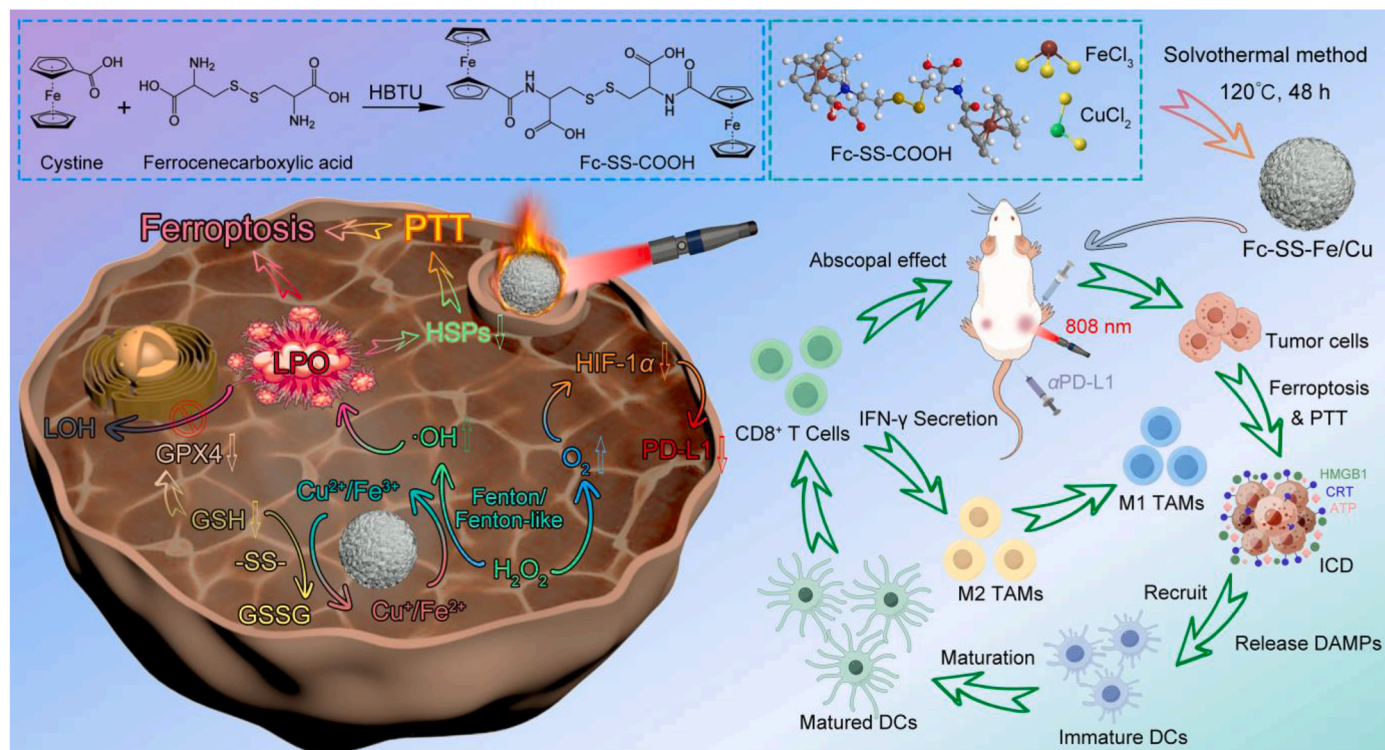
In contrast to small molecule drugs, the unique size and precisely controlled composition, structure, and functional group modifications of nanomedicines confer enhanced adaptability to TIME [31–34]. Due to the ability of ferrocene (Fc) to induce ferroptosis, bis-Fc-cystine (Fc-SS-COOH) was synthesized in this paper by introducing Fc at the

amino terminus of cystine. Furthermore, a novel nanoparticle (Fc-SS-Fe/Cu) with enhanced immune effects was successfully prepared through hydrothermal synthesis using Fe/Cu as dual coordinating metals, as depicted in Scheme 1. Fc-SS-Fe/Cu decomposes within the weak acidic environment of tumor cells, releasing Fc and dual metal ions. In its capacity as a Fenton/Fenton-like reaction catalyst, Fe^{2+} and Cu^+ effectively facilitate the conversion of H_2O_2 into $\cdot\text{OH}$. Simultaneously, disulfide bonds and generated Fe^{3+} and Cu^{2+} can deplete cellular GSH levels and downregulate GPX4 protein expression, leading to a cascade of ROS-induced oxidative stress that induces lipid peroxidation and triggers ferroptosis. Withal, the positive feedback mechanisms of "laser-triggered PTT, PTT accelerated ferroptosis and LPO accumulation, LPO mediated HSPs down-regulated to promote PTT," effectively triggers immunogenic cell death (ICD) in tumor cells, significantly enhancing their immunogenicity. Importantly, Fc-SS-Fe/Cu effectively downregulates the expression of PD-L1 protein and enhances T cell infiltration, thereby significantly augmenting the efficacy of immune checkpoint inhibitors ($\alpha\text{PD-L1}$). In summary, this combined/self-enhanced strategy elucidated a new therapeutic regimen for tumor immunotherapy.

2. Results and discussions

2.1. Structure and characterization of Fc-SS-Fe/Cu

The target molecule Fc-SS-COOH was first synthesized via HBTU-mediated amide bond formation between ferrocene and cystine, which has been confirmed by MS and $^{13}\text{C}/^1\text{H}$ NMR (Fig. S1–S3). And then, Fc-SS-Fe/Cu nanoparticles were prepared via solvothermal-method in DMF using Fc-SS-COOH and $\text{FeCl}_3/\text{CuCl}_2$. The size and morphology of Fc-SS-Fe/Cu were examined by transmission electron microscopy (TEM) and scanning electron microscopy (SEM) (Fig. 1a and b), which revealed Fc-SS-Fe/Cu exhibit the homogeneous spherical morphology with an average diameter of approximately 111.2 ± 11.9 nm. The elemental mappings (Fig. 1c) demonstrate a remarkably homogeneous distribution of S, Fe and Cu. Furthermore, the X-ray diffraction (XRD) patterns



Scheme 1. Schematic Illustration of synthetic process and therapeutic mechanism of Fc-SS-Fe/Cu.

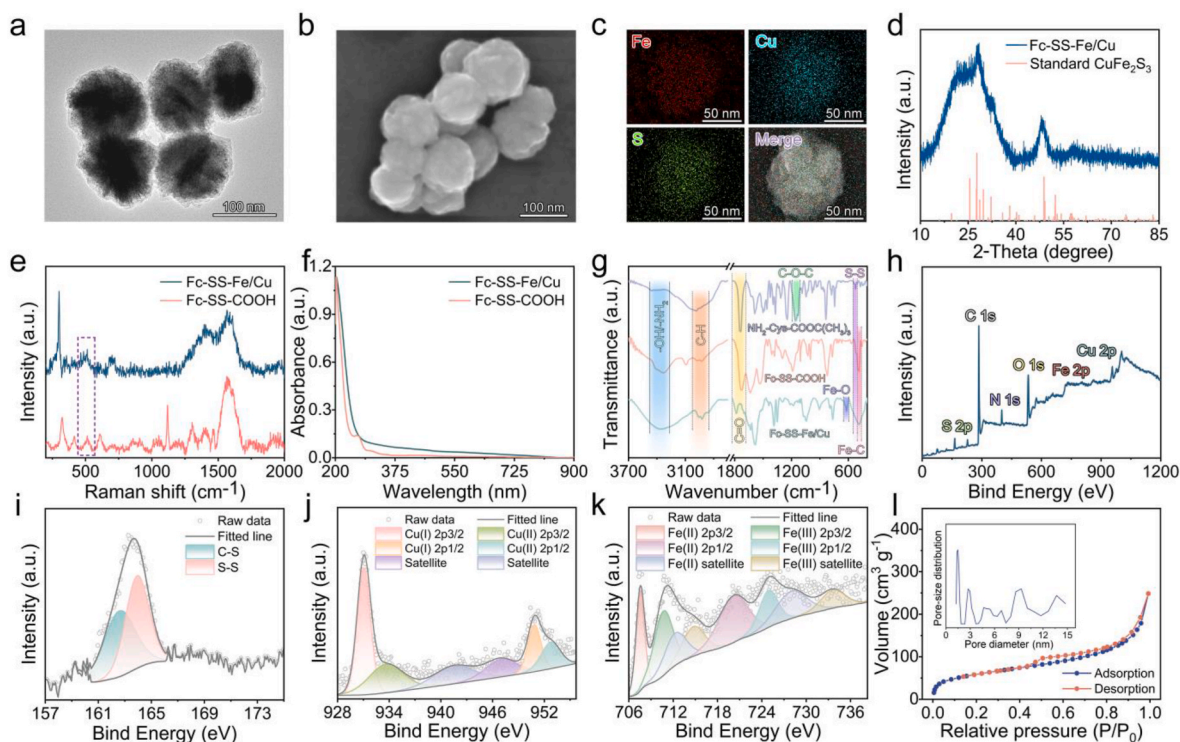


Fig. 1. (a) TEM image, (b) SEM image, (c) elemental distribution mapping, and (d) XRD spectra of Fc-SS-Fe/Cu. (e) Raman spectra and (f) absorption spectra of Fc-SS-Fe/Cu and Fc-SS-COOH. (g) FTIR spectra. (h) XPS spectrum, (i) high-resolution S 2p spectrum, (j) high-resolution Cu 2p spectrum, and (k) high-resolution Fe 2p spectrum of Fc-SS-Fe/Cu. (l) N_2 adsorption-desorption isotherms of Fc-SS-Fe/Cu.

(Fig. 1d) showed that the diffraction pattern matched with that of standard $CuFe_2S_3$ (PDF#81-1371) [35]. The Raman spectrum (Fig. 1e) showed a characteristic band corresponding to the disulfide bond at around 500 cm^{-1} , providing evidence for the successful introduction of disulfide bonds in Fc-SS-Fe/Cu [36]. In the absorption spectrum (Fig. 1f), it is evident that the absorption of Fc-SS-Fe/Cu extends into the near-infrared region in comparison to Fc-SS-COOH, which is attributed to the d-d transition and the charge transfer transition. The Fourier transform infrared spectroscopy (FTIR) shows that the broad peak at $3450\text{--}3200\text{ cm}^{-1}$ indicates the presence of a substantial number of carboxyl groups in Fc-SS-COOH (Fig. 1g). The sharp peak at 1730 cm^{-1} corresponds to the C=O stretching vibration. The S-S bond at 522 cm^{-1} and the Fe-C bond at 486 cm^{-1} provide evidence for the successful linkage between ferrocene and cysteine. However, the C=O peak of Fc-SS-Fe/Cu is red-shifted, which can be attributed to the doping of Fe/Cu and results in longer wavelengths shifting. The chemical compositions of Fc-SS-Fe/Cu were further elucidated through X-ray photoelectron spectroscopy (XPS) analysis (Fig. 1h), the full-scan spectrum exhibits diffraction peaks corresponding to S 2p, C 1s, N 1s, O 1s, Fe 2p, and Cu 2p in Fc-SS-Fe/Cu, which were determined by peaks at 163.6, 284.6, 399.6, 531.6, 716.6 and 931.6 eV, respectively. Among them, the high-resolution XPS analysis revealed that the S 2p spectrum (Fig. 1i) was further deconvoluted to two distinct peaks at 162.6 and 164.0 eV, corresponding to C-S and S-S, respectively. The four distinct peaks in the Cu 2p spectrum (Fig. 1j) at 931.1, 933.6, 950.9, and 953.2 eV correspond to $Cu^+ 2p_{3/2}$, $Cu^{2+} 2p_{3/2}$, $Cu^+ 2p_{1/2}$, and $Cu^{2+} 2p_{1/2}$, respectively. And the distinct peaks (Fig. 1k) at 707.6, 720.4, 710.8 and 725.0 eV correspond to $Fe^{2+} 2p_{3/2}$, $Fe^{2+} 2p_{1/2}$, $Fe^{3+} 2p_{3/2}$ and $Fe^{3+} 2p_{1/2}$, respectively. These findings validate the presence of dual valences of Cu and Fe elements in Fc-SS-Fe/Cu, as well as the presence of disulfide bonds. Subsequently, we employed inductively coupled plasma mass spectrometry (ICP-MS) analysis to determine the content of Cu in Fc-SS-Fe/Cu, which was found to be 2.89%, and the content of Fe was determined to be 5.12% (in mass percentage). Moreover, the

mesoporous structure of Fc-SS-Fe/Cu enhances its surface area, which was determined to be approximately $215\text{ m}^2\text{ g}^{-1}$ by the Brunauer-Emmett-Teller (BET) method (Fig. 1l), indicating its potential as a drug carrier. The increased specific surface area provides more active sites for light interaction, thereby improving light absorption and consequently enhancing the photo-thermal effect.

2.2. Photothermal Properties of Fc-SS-Fe/Cu

In order to evaluate the potential of Fc-SS-Fe/Cu as a photothermal agent for PTT, the photothermal performance was evaluated using 808 nm laser irradiation, which offers excellent tissue penetration and high energy (Fig. 2a). As shown in Fig. 2b and c, the temperature of Fc-SS-Fe/Cu increased with increasing concentration and power, demonstrating the excellent photothermal responsiveness. The photothermal conversion efficiency (η) of Fc-SS-Fe/Cu was evaluated and calculated, which was measured to be $\sim 43.89\%$ (Fig. 2d, S9 and S10). The results depicted in Fig. 2e revealed that the Fc-SS-Fe/Cu exhibited exceptional photothermal stability, as evidenced by the absence of any significant thermal decay even after several heating/cooling cycles. Under the irradiation of 808 nm laser (1.0 W cm^{-2}) for 10 min, infrared thermal imaging revealed a significant temperature increase in Fc-SS-Fe/Cu compared to dd water, with the temperature rising from 24.5°C to 47.2°C (Fig. 2f). The exceptional photothermal response and conversion performance of Fc-SS-Fe/Cu further substantiate the potential as a promising photothermal agent for tumor therapy.

2.3. Consumption of GSH

GSH plays a crucial role as a barrier in active oxygen-mediated cancer therapy by effectively scavenging exogenous ROS, thereby mitigating oxidative stress induced by ROS. As the excellent GSH scavengers, Fe^{3+}/Cu^{2+} and disulfide bond can effectively reduce the weakening degree of GSH on oxidative stress (Fig. 2a). Here, 5,5'-Dithiobis-(2-

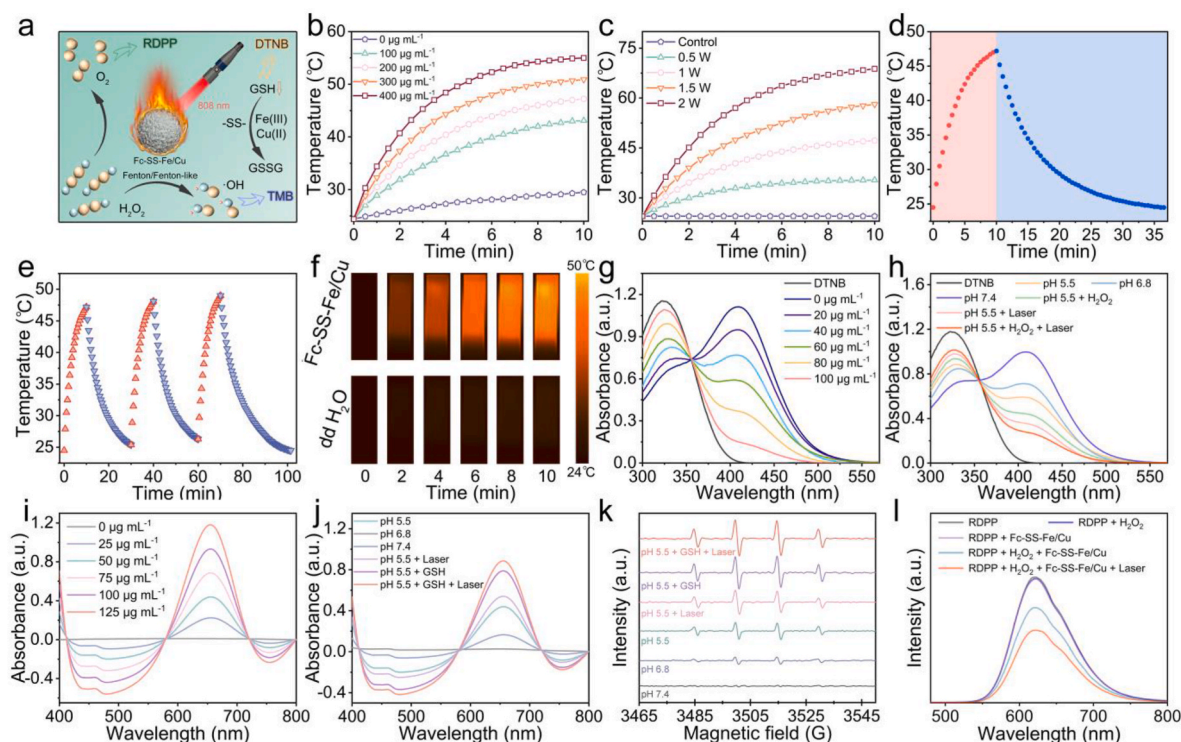


Fig. 2. (a) An illustration showing the performance mechanism of Fc-SS-Fe/Cu. (b) Temperature curves of Fc-SS-Fe/Cu subjected to laser (808 nm, 1.0 W cm⁻²) irradiation. (c) Temperature curves of Fc-SS-Fe/Cu (200 µg mL⁻¹) subjected to laser (808 nm) irradiation. (d) Temperature change curves of Fc-SS-Fe/Cu under laser irradiation (red dot line) and cooling period (blue dot line). (e) Photothermal cycling curve of Fc-SS-Fe/Cu (200 µg mL⁻¹). (f) Infrared thermal images of Fc-SS-Fe/Cu (200 µg mL⁻¹) under laser irradiation (808 nm, 1.0 W cm⁻²). (g,h) The consumption of GSH, (i,j) the production of ·OH, (k) ESR spectra of ·OH with DMPO as the capture probe and (l) the production of O₂ after different treatment.

nitrobenzoic acid) (DTNB) can be reduced to produce 5-thio-2nitrobenzoic acid (TNB) by GSH, which can be utilized for evaluating the GSH consumption ability of Fc-SS-Fe/Cu through determination of the absorption at 412 nm (Fig. S11) [37,38]. As depicted in Fig. 2g, a significant decrease in absorbance at 412 nm was observed with increasing concentrations of Fc-SS-Fe/Cu, indicating efficient GSH consumption by Fc-SS-Fe/Cu. In comparison to the conditions of other experiments (Fig. 2h), the consumption of GSH was most pronounced when laser irradiation was applied under conditions simulating the tumor micro-environment (weak acidity + H₂O₂). This is attributed to the ability of low-valent metals to undergo oxidation to high-valent states in the presence of H₂O₂, thereby enhancing the consumption of GSH, which can be further potentiated through photo-thermal mechanisms.

2.4. Generation of ·OH and O₂

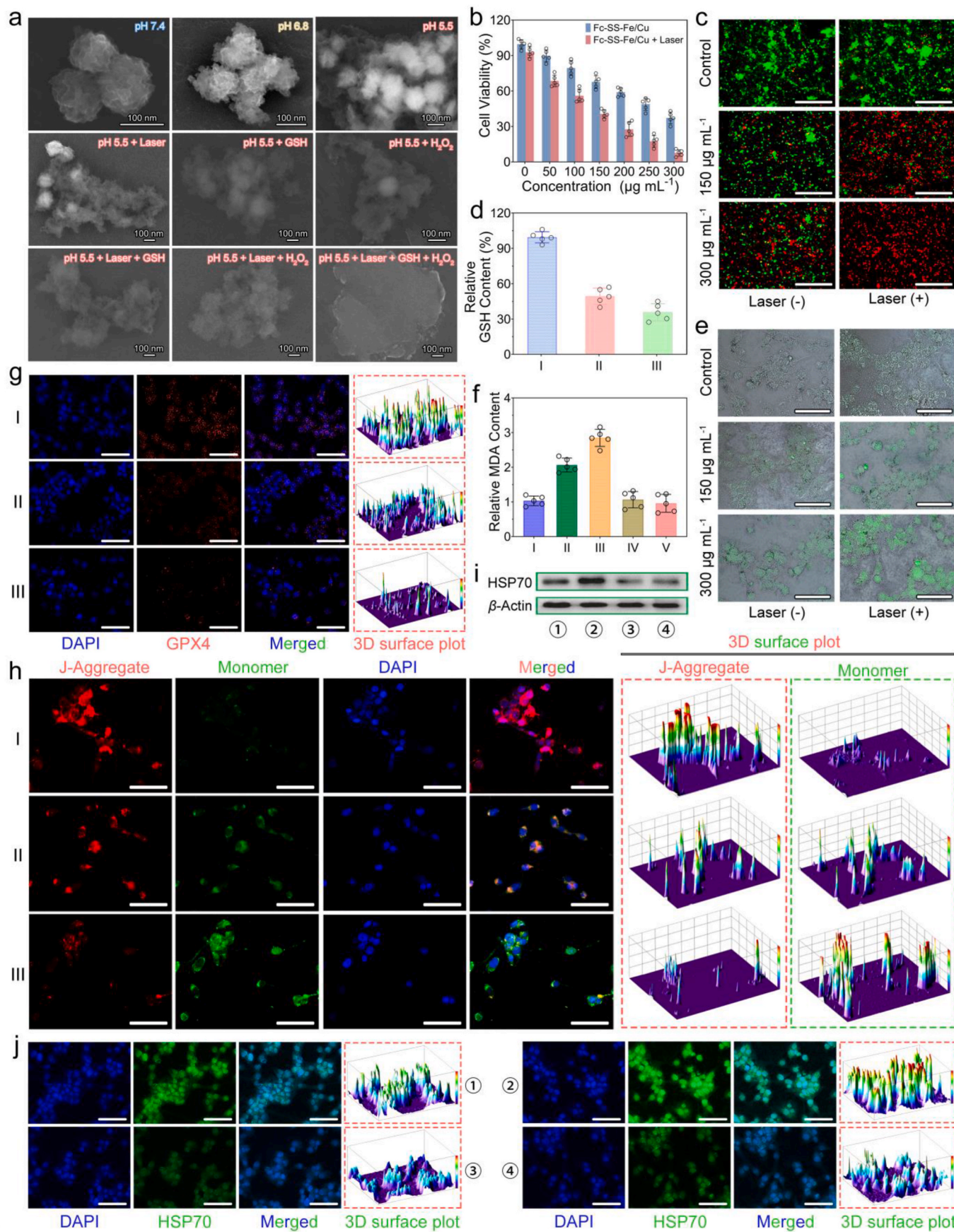
The generation of ·OH through the Fenton/Fenton-like reaction is a crucial mechanism for inducing ROS-mediated oxidative stress (Fig. 2a). Here, 3,3',5,5'-Tetramethylbenzidine (TMB) was employed as a probe to evaluate the capability of Fc-SS-Fe/Cu in generating ·OH (Fig. S12) [39, 40]. As shown in Fig. 2i, the generation of ·OH gradually increases with the increase of Fc-SS-Fe/Cu concentration. Furthermore, acidity and laser irradiation promote the Fenton/Fenton-like reaction of Fc-SS-Fe/Cu to generate ·OH (Fig. 2j). Interestingly, following GSH pretreatment, a greater amount of ·OH was generated, attributed to the capacity of GSH to efficiently reduce high-valent metals to low-valence, thereby augmenting the production of ·OH. Moreover, these findings were further validated through electron spin resonance (ESR) spectroscopy, as depicted in Fig. 2k. The above analysis reveals that the triple response of Fc-SS-Fe/Cu to pH/GSH/laser can synergistically enhance the Fenton/Fenton-like reaction, leading to increased generation of ·OH. The redox cycling of metal valence provides continuous driving force for

GSH consumption and ·OH generation.

The other significant impact of the Fenton/Fenton-like reaction is the generation of O₂. In this study, we employed [Ru(dpp)₃]Cl₂ (RDPP) to validate the O₂-generating capability of Fc-SS-Fe/Cu, which is a specific and dynamic fluorescence probe for O₂, with its fluorescence intensity at 615 nm exhibiting an inverse correlation with the O₂ concentration [41]. As shown in Fig. 2l, the fluorescence intensity of RDPP remained unchanged in the absence of H₂O₂ or Fc-SS-Fe/Cu, indicating a lack of expected O₂ production. However, when both H₂O₂ and Fc-SS-Fe/Cu were present, the fluorescence intensity of RDPP was significantly reduced, suggesting the generation of O₂. Moreover, under laser exposure, the reduction in fluorescence intensity of RDPP is more pronounced, providing evidence that the photothermal heating effect can significantly enhance O₂ generation.

2.5. Biodegradation behavior

The biodegradability of nanomedicine for anti-tumor treatment should be considered a critical indicator to ensure therapeutic efficacy and drug safety [42–44]. In theory, the disulfide bonds would undergo cleavage in the reducing environment, while under acidic conditions, Fe/Cu ions would be liberated with unbound state, resulting in the degradation of the structure [45–48]. To validate this hypothesis, we performed direct observations of the biodegradability of Fc-SS-Fe/Cu in a simulated TME by SEM (Fig. 3a). Under neutral conditions, the structural integrity of Fc-SS-Fe/Cu remains predominantly intact; however, exposure to acidic conditions (pH 5.5) leads to significant collapse of some Fc-SS-Fe/Cu within a span of 12 h. Moreover, when subjected to simultaneous laser irradiation in the presence of GSH and H₂O₂, the framework of Fc-SS-Fe/Cu undergoes complete collapse, which is attributed to the fact that the metal ions and disulfide bonds of Fc-SS-Fe/Cu can effectively react with GSH and H₂O₂ under acidic



(caption on next page)

Fig. 3. (a) SEM images of Fc-SS-Fe/Cu after different treatments for 12 h. (b) The cell viabilities of CT26 cells after treatment. Data presented as mean \pm SD (n=5). (c) CLSM images of CT26 cells stained with Calcein AM/PI after treatment, scale bar: 200 μ m. (d) The GSH content of CT26 cells. Treatments included: I: PBS, II: Fc-SS-Fe/Cu, III: Fc-SS-Fe/Cu + Laser. Data presented as mean \pm SD (n=5). (e) DCFH-DA staining of CT26 cells, scale bar: 50 μ m. (f) Intracellular MDA content. Treatments included: I: PBS, II: Fc-SS-Fe/Cu, III: Fc-SS-Fe/Cu + Laser, IV: Fc-SS-Fe/Cu + Fer-1, V: Fc-SS-Fe/Cu + Laser + Fer-1. Data presented as mean \pm SD (n=5). (g) GPX4 expression analyzed with immunofluorescence assay, scale bar: 50 μ m. Treatments included: I: PBS, II: Fc-SS-Fe/Cu, III: Fc-SS-Fe/Cu + Laser. (h) CLSM images depicting the alterations in intracellular MMPs, as visualized through JC-1 staining presented after undergoing different treatments, scale bars: 50 μ m. Treatments included: I: PBS, II: Fc-SS-Fe/Cu, III: Fc-SS-Fe/Cu + Laser. HSP70 expression analyzed with (i) western blot and (j) immunofluorescence assay, scale bar: 50 μ m. Treatments included: ① PBS, ② 45°C, ③ Fc-SS-Fe/Cu, ④ Fc-SS-Fe/Cu + Laser.

conditions, leading to structural collapse, and it can also be further accelerated by the photothermal effect.

2.6. *In vitro* cytotoxicity assay

We subsequently evaluated the therapeutic efficacy of Fc-SS-Fe/Cu using the Cell Counting Kit 8 (CCK-8) assay, which assessed the cytotoxicity against CT26 mouse colon cancer cells, 4T1 mouse breast cancer cells, Hela human cervical cancer cells, MCF-7 human breast cancer cells, HepG2 human liver cancer cells and L929 mouse normal cells. As shown in Fig. 3b, Fc-SS-Fe/Cu exhibited dose-dependent cytotoxicity against CT26 cells, with a significant decrease in cell viability under 808 nm laser irradiation, demonstrating the photothermal therapeutic capability of Fc-SS-Fe/Cu. Moreover, other tumor cells also presented a similar effective cytotoxicity trend. (Fig. S13). However, for L929 cells, the cytotoxicity remained within an acceptable range (Fig. S14). This disparity can be attributed to the weak acidic TME, as well as the elevated expression levels of GSH and H₂O₂ in tumor cells. Moreover, we employed Calcein-AM and propidium iodide staining to assess the efficacy of multiple therapies. As shown in Fig. 3c, compared to other treatment methods, the combination therapy of Fc-SS-Fe/Cu and PTT exhibited the strongest cytotoxicity, which is consistent with the CCK8 results.

2.7. Intracellular depletion of GSH and generation of \cdot OH

To further investigate the consumption of intracellular GSH by Fc-SS-Fe/Cu, we quantified the relative content of intracellular GSH using a GSH assay kit. As depicted in Fig. 3d, at a concentration of 300 μ g mL⁻¹, approximately 50% of intracellular GSH has been depleted. However, upon exposure to additional 808 nm laser irradiation, around 65% of GSH can be consumed. It can be attributed to the ability of high-valence metal ions (Fe³⁺/Cu²⁺) liberated from collapsed Fc-SS-Fe/Cu and disulfide bonds in organic ligands to consume GSH, and the reaction rate could be accelerated by the photothermal effect. Here, 2',7'-Dichlorofluorescein diacetate (DCFH-DA) was used as a fluorescent probe to reflect the levels of intracellular \cdot OH. As shown in Fig. 3e, the cells exhibited relatively strong green fluorescence after treatment with Fc-SS-Fe/Cu, and a stronger signal appeared under the additional laser irradiation, which can be attributed to the ability of Fe²⁺/Cu⁺ and Fc to produce \cdot OH through the Fenton/Fenton-like reaction, which is also further enhanced by the photothermal effect.

2.8. Fc-SS-Fe/Cu could induce ferroptosis

The increased intracellular oxidative stress, caused by higher levels of ROS and lower levels of GSH, was a theoretical basis for the effective induction of ferroptosis. Here, the occurrence of ferroptosis was verified by quantifying the intracellular relative levels of LPO using the MDA detection kit. The CT26 cells were subjected to individual treatments with PBS, Fc-SS-Fe/Cu, Fc-SS-Fe/Cu + Laser, Fc-SS-Fe/Cu + Fer-1 (Ferrostatin-1, a classical ferroptosis inhibitor), Fc-SS-Fe/Cu + Laser + Fer-1, respectively. As shown in Fig. 3f, compared to the control group, the LPO significantly increased in Fc-SS-Fe/Cu treatment and was further enhanced by laser irradiation, which can be attributed to the promotion of Fenton/Fenton-like reactions through photothermal effect. Importantly, no significant increase in LPO was observed after

additional treatment with Fer-1, indicating that Fer-1 inhibited the occurrence of ferroptosis induced by Fc-SS-Fe/Cu and suggesting that Fc-SS-Fe/Cu could effectively mediate ferroptosis in CT26 cells. GSH-GPX4 pathway plays a crucial role in inhibiting ferroptosis by defending against oxidative stress. As another marker of ferroptosis, the expression level of GPX4 can effectively reflect the detoxification effect on LPO. In this paper, the expression of GPX4 was investigated by immunofluorescence assay analysis, as depicted in Fig. 3g, the expression of GPX4 was significantly reduced in CT26 cells treated with Fc-SS-Fe/Cu and further decreased under additional laser irradiation, which can be attributed to the effective reduction of GPX4 expression through the consumption of GSH by Fc-SS-Fe/Cu. Furthermore, ferroptosis is frequently accompanied by mitochondrial dysfunction, characterized by a significant reduction in mitochondrial membrane potential (MMP), which serves as a pivotal indicator [49–51]. Here, JC-1 was used as a probe to measure MMP, as shown in Fig. 3h, the healthy mitochondria exhibited red fluorescence, whereas upon treatment with Fc-SS-Fe/Cu, the cells demonstrated a reduction in red fluorescence intensity accompanied by an increase in green fluorescence signal. Furthermore, this effect was further potentiated upon exposure to laser irradiation, indicating that Fc-SS-Fe/Cu induced significant mitochondrial damage under laser irradiation. Therefore, in conclusion, Fc-SS-Fe/Cu exhibit a pronounced ability to induce ferroptosis.

2.9. Fc-SS-Fe/Cu enhanced PTT effect by down-regulating HSPs

At temperatures exceeding the body temperature by 5°C or more, cancer cells will elicit a stress response and exhibit abnormal over-expression of HSPs to augment their heat tolerance and stability [52,53]. In particular, HSP70 plays a significant role in aiding cancer cells to withstand adverse environments and repair cell damage caused by PTT. Thus, effectively downregulating the expression of HSPs in cancer cells can potentiate the therapeutic efficacy of mild-temperature PTT [54]. It has been reported that the inducers (ROS and LPO) of ferroptosis have demonstrated the capability to effectively downregulate the expression of HSPs [23,26,27]. This finding provides an extremely important basis for the combined application of ferroptosis and PTT. To explore the impact of Fc-SS-Fe/Cu-induced ferroptosis on HSPs expression, we assessed the expression levels of HSP70 in cancer cells through western blotting analysis. As depicted in Fig. 3i, compared to the control group, tumor cells exhibited heightened HSP70 expression under elevated temperature, whereas its expression was notably diminished in the Fc-SS-Fe/Cu treatment group, demonstrating that Fc-SS-Fe/Cu-induced elevation of LPO and ROS effectively suppresses HSP70 expression. Notably, co-treatment with Fc-SS-Fe/Cu and PTT did not result in conspicuous overexpression of HSP70. Subsequently, we further corroborated this finding by immunofluorescence staining (Fig. 3j), yielding consistent results that robustly support the notion that ferroptosis can efficiently inhibit HSPs expression, offering a promising avenue for enhancing mild-temperature PTT.

2.10. Immune activation effect of Fc-SS-Fe/Cu

Recent studies have demonstrated that ferroptosis and PTT can effectively induce immunogenic cell death (ICD), characterized by the release of damage-associated molecular patterns (DAMPs), mainly including calreticulin (CRT), high mobility group box 1 (HMGB1) and

adenosine triphosphate (ATP) [55–59]. As an "eat me" signaling protein, CRT can undergo transport to the cell membrane for recognition and binding by dendritic cells during the early stages of ICD. In this study, anti-CRT-AF488 was used as an immunofluorescence probe to reflect the CRT on the surface of cell membrane. As shown in Fig. 4a, compared with other treatment groups, the extracellular green fluorescence was the strongest after Fc-SS-Fe/Cu combined with PTT treatment, indicating that a large amount of CRT was transferred to the extracellular membrane. As an inflammatory cytokine, HMGB1 predominantly localizes within the nucleus; however, during the intermediate and late stages of ICD, HMGB1 is released from the nucleus to initiate the activation of inflammatory responses. As depicted in Fig. 4b, HMGB1 exhibited prominent nuclear localization in both the PBS group and PBS + Laser group. However, treatment with Fc-SS-Fe/Cu and additional laser irradiation resulted in the enhanced release of HMGB1. Furthermore, analysis of HMGB1 content in the culture supernatant revealed significantly higher levels in the Fc-SS-Fe/Cu and Fc-SS-Fe/Cu + Laser groups, indicating that Fc-SS-Fe/Cu combined with PTT treatment could synergistically promote HMGB1 release from tumor cells (Fig. 4c). Moreover, ATP functions as a "find me" signaling that can promote infiltration of effector T cells, which can be released during the intermediate and early stages of ICD. As shown in Fig. 4d, the secretion of ATP was significantly higher in the Fc-SS-Fe/Cu group compared to the PBS group and PBS + Laser group, with even more pronounced effects when combined with PTT. In summary, Fc-SS-Fe/Cu combined

with PTT can effectively induce ICD by promoting CRT exposure, HMGB1 release, and ATP secretion, thereby activating the immune response.

2.11. Fc-SS-Fe/Cu decreased HIF-1 α and PD-L1 levels

The hypoxic microenvironment of tumors, as a significant immune-related adverse event, confers upon tumors the capacity to promote metastasis and drug resistance, particularly by upregulating HIF-1 α expression induced by hypoxia, thereby resulting in increased PD-L1 expression [60]. Thus, effectively suppressing the expression of HIF-1 α offers the potential for selectively inhibiting the expression of PD-L1 [61]. Based on the oxygen-generating ability of Fc-SS-Fe/Cu, we assessed the expression of HIF-1 α through immunofluorescence staining. As depicted in Fig. 4e, exposure to light alone did not induce a significant change in the expression of HIF-1 α compared to the control group. However, following treatment with Fc-SS-Fe/Cu, a noticeable reduction in HIF-1 α expression was observed, which was further diminished after PTT. These findings indicate that the Fc-SS-Fe/Cu-mediated O₂ generation could effectively attenuate cellular HIF-1 α expression. Based on the co-expression characteristics of HIF-1 α and PD-L1, we employed immunofluorescence staining to track the expression levels of PD-L1. Encouragingly, the trend of PD-L1 expression was consistent with that of HIF-1 α (Fig. 4f). Consequently, the co-inhibition of HIF-1 α and PD-L1 expression by Fc-SS-Fe/Cu endows

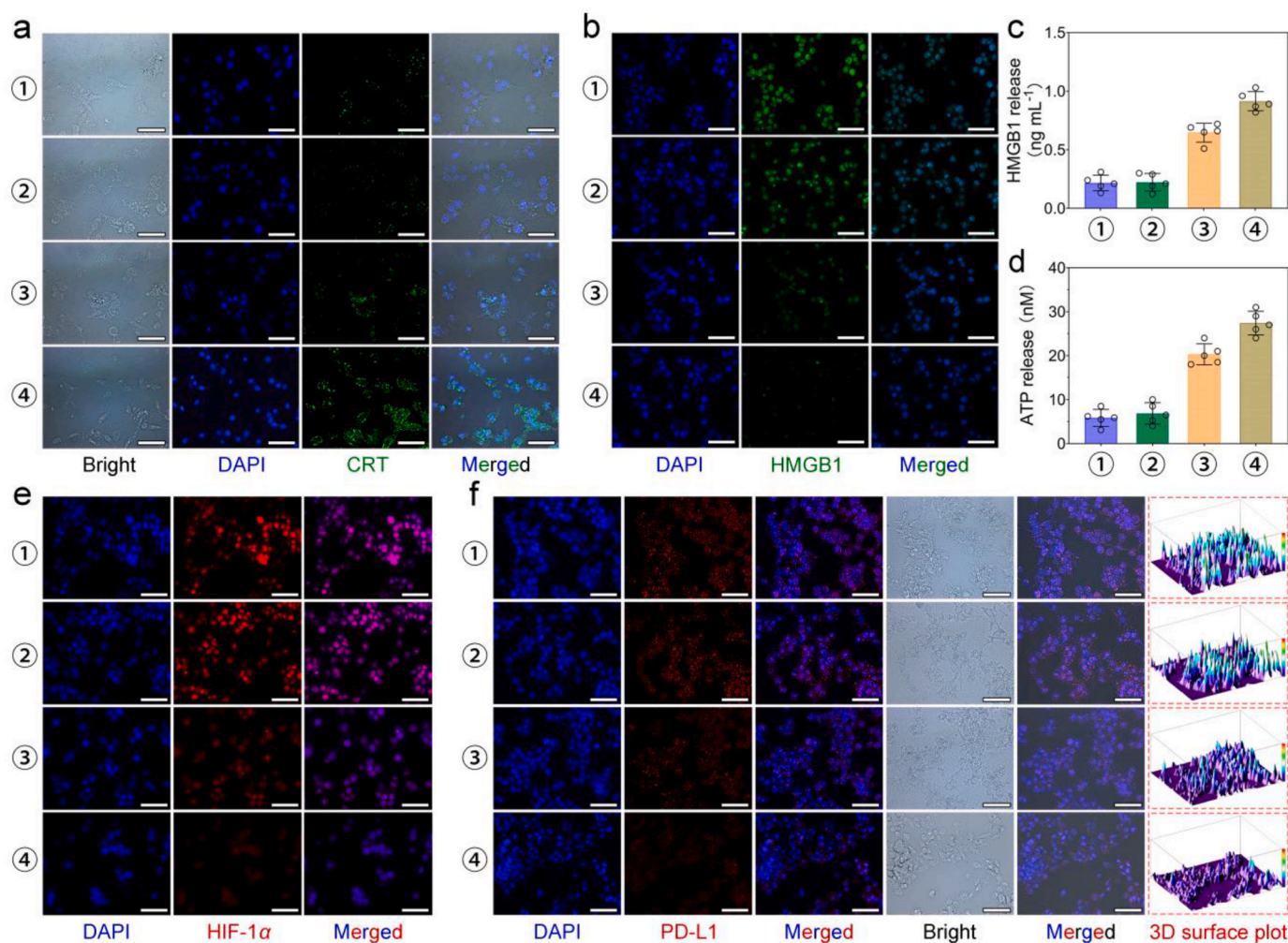


Fig. 4. (a) CRT and (b) HMGB1 of CT26 cells were determined by immunofluorescence assay, scale bar: 50 μ m. The release of (c) HMGB1 and (d) ATP after different treatment. Data presented as mean \pm SD (n=5). (e) HIF-1 α and (f) PD-L1 of CT26 cells were determined by immunofluorescence assay, scale bar: 50 μ m. The groups were as follows: ① PBS, ② PBS + Laser, ③ Fc-SS-Fe/Cu, ④ Fc-SS-Fe/Cu + Laser.

with powerful immunotherapeutic potential and provides the robust support for the effectiveness of ICB therapy.

2.12. *In vivo* anticancer activity

To establish the experimental protocol for assessing the *in vivo* anti-tumor efficacy of Fc-SS-Fe/Cu combined PTT, we employed a BALB/c mouse model to determine the initiation of PTT by monitoring the accumulation of Cy5.5-modified Fc-SS-Fe/Cu within tumors. As illustrated in Fig. S15, the highest level of enrichment was observed at the tumor site 12 h following intravenous administration. Subsequently, tissue samples from the liver, heart, lung, kidney, spleen, and tumor

were obtained through dissection of mice treated for 12 h. Fluorescence imaging reveals a significantly stronger fluorescence signal in the tumor tissue compared to other organs, indicating potential accumulation of Fc-SS-Fe/Cu at the tumor tissue site *via* the Enhanced Permeability and Retention (EPR) effect following intravenous injection for 12 h, thus establishing the initiation time for PTT synergistic therapy.

Given the promising anti-tumor effects observed *in vitro* with the Fc-SS-Fe/Cu combined PTT, we established the subcutaneous CT26 tumor BALB/c mouse model to assess the therapeutic efficacy *in vivo*. Upon reaching a tumor volume of 120 mm³, the mice were randomly allocated into three groups and treated with saline (Control), Fc-SS-Fe/Cu, and Fc-SS-Fe/Cu + Laser, respectively. As shown in the treatment plan (Fig. 5a),

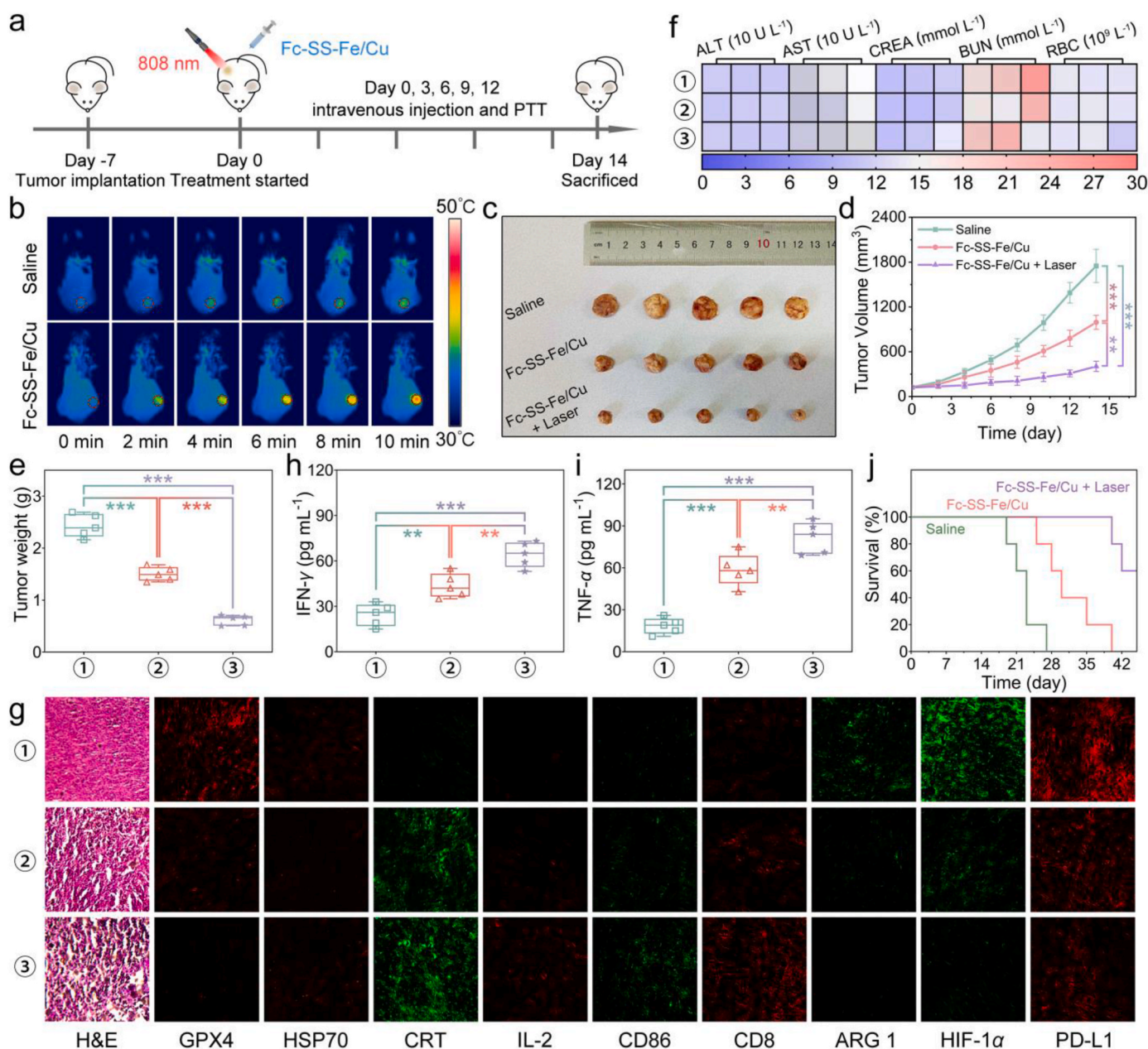


Fig. 5. *In vivo* antitumor effect evaluation. (a) Schematic illustration of tumor treatments. (b) *In vivo* thermal imaging of mice under NIR laser (808 nm, 1.0 W cm⁻²) (c) Digital photos of the tumors dissected from all the groups. (d) Tumor volume quantification during the treatment cycle. (e) Tumor weight quantification after different treatment. (f) Biochemical analysis of blood collected from mice after different treatment (alanine aminotransferase (ALT), aspartate aminotransferase (AST), creatinine (CREA), blood urea nitrogen (BUN) and red blood cell counts (RBC)). (g) H&E staining of the tumor slices and immunofluorescence images stained by GPX4, HSP70, CRT, IL-2, CD86, CD8, ARG 1, HIF-1 α and PD-L1. (h) IFN- γ content in mice serum after treatment. (i) TNF- α content in mice serum after treatment. (j) Survival rate of mice with different treatments. The groups were as follows: ① PBS, ② Fc-SS-Fe/Cu, ③ Fc-SS-Fe/Cu + Laser (n.s. means no significance, *** p<0.001, ** p<0.01, and * p<0.05).

systematic therapy was administered at three-day intervals, with tumor volume changes assessed every two days. The temperature changes of tumors were recorded using an infrared thermal imaging camera. As depicted in Fig. 5b, the tumor site treated with Fc-SS-Fe/Cu exhibited a significant temperature increase from 36.7°C to 45.9°C under laser irradiation (808 nm, 1.0 W cm⁻²), whereas the saline group only experienced a modest rise from 36.7°C to 38.5°C, highlighting the exceptional PTT ability of Fc-SS-Fe/Cu *in vivo*. During the course of treatment, it was observed that the tumor growth rate in the control group of mice was remarkably rapid, with a volume reaching 15 times its initial size. Notably, mice treated with Fc-SS-Fe/Cu exhibited a notable inhibitory effect on tumor growth. Furthermore, when combined with PTT, there was a strong suppression of tumor growth in mice, consistent with the findings from *in vitro* cell experiments (Fig. 5c–e). After 14 days of treatment, we collected mouse blood for biochemical analysis, which primarily included the assessment of alanine aminotransferase (ALT), aspartate aminotransferase (AST), creatinine (CREA), blood urea nitrogen (BUN), and red blood cell counts (RBC). The heat map of hematological and biochemical parameters in mice reveals no significant abnormalities between the experimental groups, indicating that Fc-SS-Fe/Cu exhibited favorable biocompatibility and was suitable for intravenous administration (Fig. 5f). By detecting the Cu content in the urine and feces of mice using ICP-MS, it is found that the Cu content in urine and feces was relatively abundant at 24 h post-administration and then it decreased after 48 h (Fig. S16). This indicates that Fc-SS-Fe/Cu can be effectively metabolized by the liver and kidneys and eliminated from the body through urine and feces. Additionally, throughout the entire treatment period, no significant changes in the body weight of the mice were observed (Fig. S17). Thus, these results all suggest that the therapeutic regimen employed exhibited minimal negative effects on their overall health. The hematoxylin and eosin (H&E) staining of the various organ and tumor samples revealed no significant damage to the organ tissues in each treatment group (Fig. S18). However, tumors subjected to Fc-SS-Fe/Cu combined PTT exhibited substantial tissue damage, indicating that Fc-SS-Fe/Cu significantly inhibits tumor proliferation. Given the *in vitro* experimental findings demonstrating the effective activation of ferroptosis and reduction in HSP70 protein expression by Fc-SS-Fe/Cu, we proceeded to assess its *in vivo* effects through immunofluorescence staining of tumor tissues. As depicted in Fig. 5g, Fc-SS-Fe/Cu significantly decreased the expression of GPX4 and HSP70 proteins. Moreover, the findings pertaining to CRT, HIF-1 α , and PD-L1 were also consistent with the observed trends in the *in vitro* experiment. These results indicate that the treatment of Fc-SS-Fe/Cu combined PTT could effectively trigger ICD, while the O₂-generating ability further suppresses the expression of HIF-1 α and PD-L1, which indicate promising potential for immunotherapy using this treatment approach.

To further investigate the levels of immune activation facilitated by Fc-SS-Fe/Cu, we conducted immunofluorescence analysis to detect interleukin-2 (IL-2), a cytokine that promotes T cell differentiation [62, 63]. The results revealed heightened expression of IL-2 in tumors treated with Fc-SS-Fe/Cu combined PTT, indicating a significant enhancement in lymphocyte growth, proliferation, and differentiation at this stage. CD86 serves as a robust indicator of mature dendritic cells (DCs), with its increased expression signifying the effective activation of DC maturation by Fc-SS-Fe/Cu combined PTT, thereby resulting in efficient T cell activation [64,65]. Notably, CD8⁺ T cells, as pivotal T lymphocytes, serve as essential indicators for evaluating the efficacy of immunotherapy. The immunofluorescence detection results indicated that the Fc-SS-Fe/Cu + Laser group exhibited elevated expression levels of CD8, suggesting that T lymphocytes were in the "positive" state and indicating that the immune response has been activated by Fc-SS-Fe/Cu combined PTT. The cytotoxic activity of CD8⁺ T cells is largely reliant on the production of IFN- γ [66]. Here, we conducted an ELISA assay to measure the levels of IFN- γ , and the results revealed a significantly higher secretion of IFN- γ in the Fc-SS-Fe/Cu + Laser group compared to others, consistent with the aforementioned findings (Fig. 5h). Furthermore, the

released IFN- γ can induce inflammatory responses, leading to polarization of tumor-associated macrophages (TAMs) towards the anti-tumor M1 phenotype, thereby facilitating infiltration of CD8⁺ T cells and restricting tumor immune evasion [67]. To further confirm the polarization of M2-type TAMs to M1-type, we examined M1-type related cytokine (Necrosis Factor α , TNF- α) and the expression of M1-type related indicator (CD86) as well as M2-type related protein (Arginase 1, ARG1) [68–70]. As shown in Fig. 5g and i, it can be clearly observed that in the Fc-SS-Fe/Cu + Laser group, the expression of CD86 was significantly increased compared to other treatment groups, while the expression of ARG1 was decreased. Moreover, importantly, the secretion of TNF- α in serum was also notably enhanced. This demonstrates that the combination of Fc-SS-Fe/Cu and photothermal therapy can effectively transform M2-type TAMs into M1-type. Moreover, we investigated the survival outcomes of mice, as illustrated in Fig. 5j, where all mice in the control group succumbed within 27 days. Conversely, a majority of mice in the Fc-SS-Fe/Cu + Laser group exhibited extended survival beyond 45 days, indicating that Fc-SS-Fe/Cu combined PTT significantly extended the lifespan of mice and provided compelling evidence for *in vivo* anti-tumor efficacy.

2.13. Fc-SS-Fe/Cu induced PD-L1 downregulation *in vivo*

In vitro experiments, we validated that Fc-SS-Fe/Cu could significantly induce the downregulation of PD-L1 expression on the cell surface. However, while a similar trend was observed *in vivo*, the extent of downregulation was relatively diminished, possibly attributable to the upregulation of PD-L1 by a substantial amount of IFN- γ induced through immune activation (Fig. 6a) [7,8]. To examine this hypothesis, we established CT26 bilateral tumor bearing mice and divided into 4 treatment groups: Saline, Saline + anti-IFN- γ , Fc-SS-Fe/Cu, and Fc-SS-Fe/Cu + anti-IFN- γ (Fig. 6b). Here, the neutralizing antibody (anti-IFN- γ) was used to counteract the abundant IFN- γ *in vivo*, and the tumor on the right side was irradiated with laser (808 nm, 1.0 W cm⁻²). Following three treatment cycles, the mice were euthanized and the tumors were subjected to HIF-1 α and PD-L1 immunofluorescence staining. As shown in Fig. 6c, compared to the Saline group, the expression of HIF-1 α was significantly reduced after treatment with Fc-SS-Fe/Cu, particularly when combined with PTT. However, the suppression of PD-L1 was not as pronounced as that of HIF-1 α . In comparison to Fc-SS-Fe/Cu and Saline + anti-IFN- γ groups, Fc-SS-Fe/Cu + anti-IFN- γ group exhibited significant suppression of PD-L1 expression. It can be inferred that the immune activation triggered by traditional ICD leads to the release of IFN- γ , which enhances the expression of PD-L1. Excitingly, Fc-SS-Fe/Cu with PTT not only effectively activate the immune system but also efficiently suppress the expression of HIF-1 α by O₂ generation, thereby relatively inhibiting the expression of PD-L1. Therefore, Fc-SS-Fe/Cu represents a highly suitable nanomedicine for PD-L1-mediated ICB therapy.

2.14. Bilateral antitumor activity by Fc-SS-Fe/Cu

To further confirm the functionality of the anti-tumor immune response induced by Fc-SS-Fe/Cu combined Laser, we investigated the synergistic effect of combined immune checkpoint inhibitor (α PD-L1) *in vivo* by establishing the dual tumor mouse model. The tumor on the right side was treated with intra-tumoral injection as the primary lesion, and the left side was treated as the distant metastasis. The treatment method is illustrated in Fig. 7a. Upon reaching a tumor volume of 120 mm³, CT26 bilateral tumor bearing mice were randomly divided into 5 groups, which were treated with saline, α PD-L1, Fc-SS-Fe/Cu, Fc-SS-Fe/Cu + Laser, and Fc-SS-Fe/Cu + Laser + α PD-L1, respectively. After a 14-day treatment, the mice were euthanized and bilateral tumors as well as visceral organs were dissected. As shown in Fig. 7b–e, the monotherapy of α PD-L1 failed to exhibit significant tumor suppression, which was limited by insufficient immunogenicity and inadequate immune

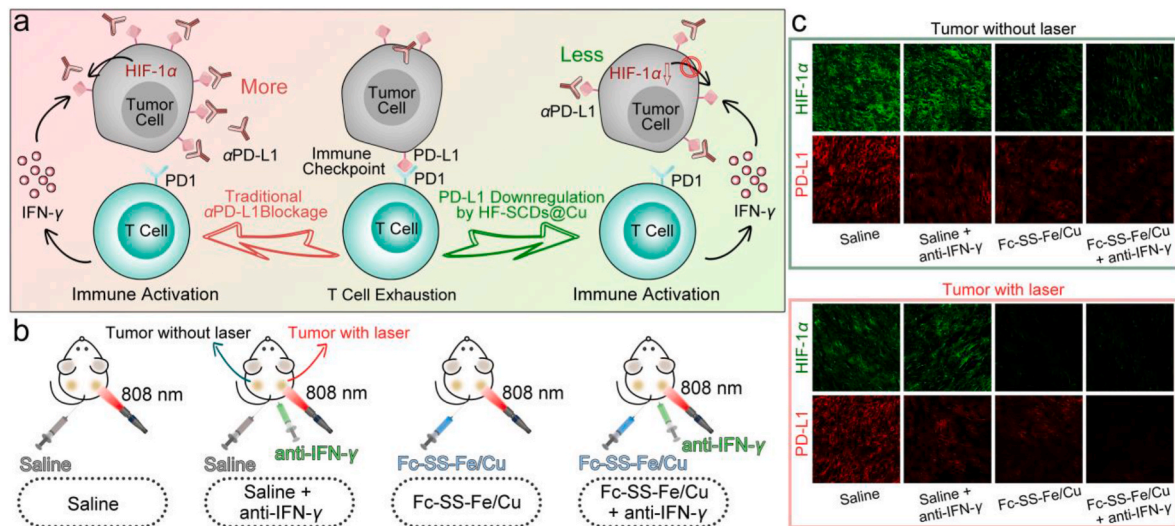


Fig. 6. Fc-SS-Fe/Cu induced PD-L1 downregulation *in vivo*. (a) Illustration of PD-L1 downregulation caused by Fc-SS-Fe/Cu. (b) Schematic illustration of tumor treatment model. (c) Immunofluorescence images of the tumor slices stained by HIF-1 α and PD-L1.

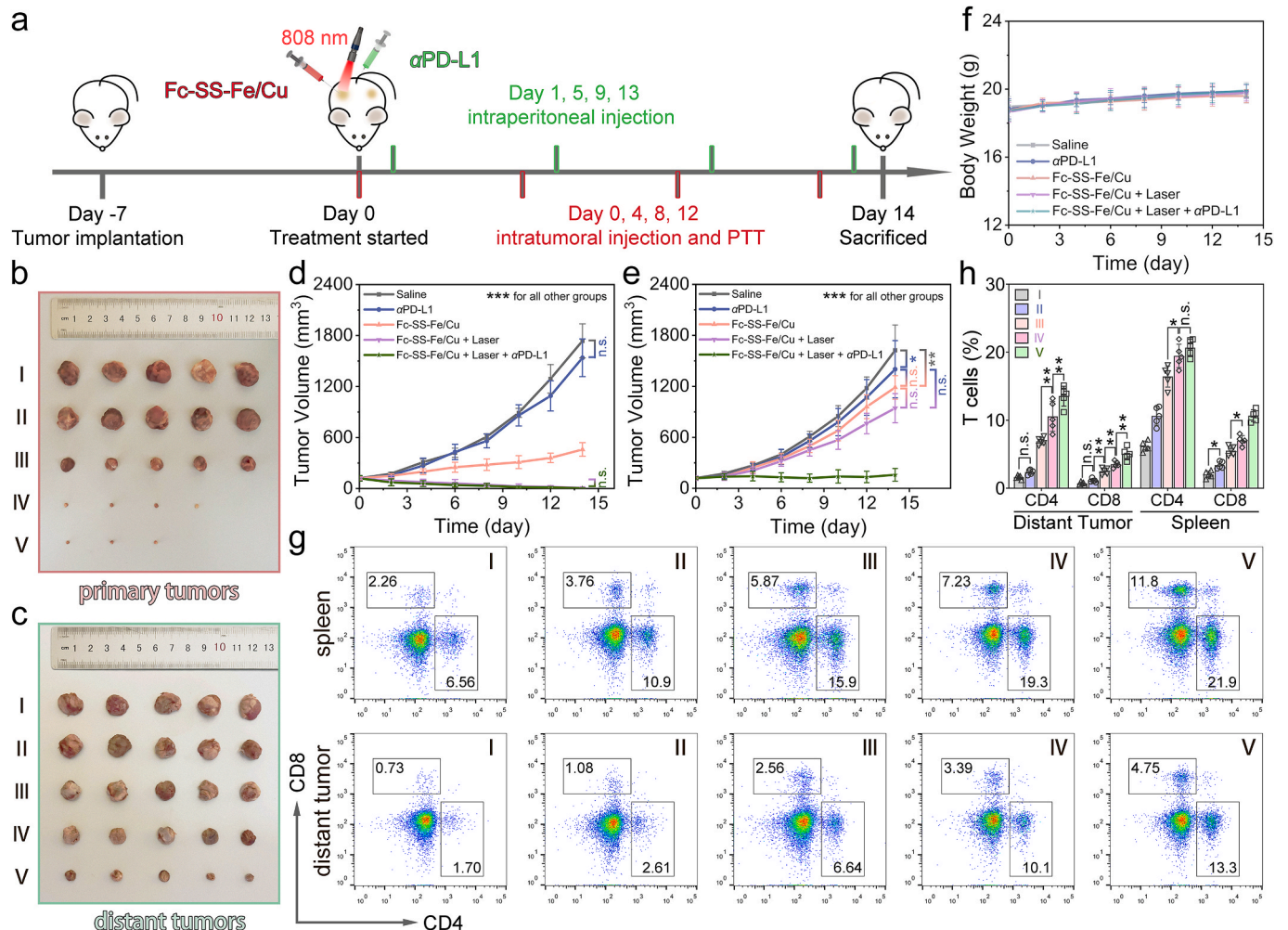


Fig. 7. Antitumor immune effects of Fc-SS-Fe/Cu in combination with α PD-L1. (a) Therapeutic schedule of the *in vivo* antitumor treatment. (b) Image of primary tumors after different treatments. (c) Image of distant tumors after different treatments. (d) Primary tumor volume of the treated mice in different groups. (e) Distant tumor volume of the treated mice in different groups. (f) Body weight of BALB/c mice changes during treatment. (g) Representative flow cytometry plots showing different groups of T cells in distant tumor and spleen of dual-tumor-model mice. (h) The percentage of T cells in the distant tumor and spleen of dual-tumor-model mice tested by flow cytometry (n.s. means no significance, *** $p < 0.001$, ** $p < 0.01$, and * $p < 0.05$).

infiltration. However, the Fc-SS-Fe/Cu + Laser and Fc-SS-Fe/Cu + Laser + α PD-L1 groups exhibited a highly significant inhibition of tumor proliferation in the primary tumor. For distant tumors, we observed that the Fc-SS-Fe/Cu + Laser group demonstrated ideal tumor growth inhibition compared to the control group. Excitingly, the Fc-SS-Fe/Cu + Laser + α PD-L1 group demonstrated a remarkably significant inhibition of tumor growth, which was due to the effective activation of immunogenicity and the reduction of PD-L1 expression on the surface of tumor cells by Fc-SS-Fe/Cu combined PTT, further enhancing the efficacy of α PD-L1. Moreover, there was no significant change in the body weight of mice observed during the treatment period (Fig. 7f), and histological examination using H&E staining (Fig. S19) revealed uniform organ density with no apparent damage across all experimental groups. In addition, we further analyzed the proportions of CD4⁺ T cells and CD8⁺ T cells in the spleen and tumor of mice by flow cytometry to reflect the degree of immune activation. As illustrated in Fig. 7g and h, the Fc-SS-Fe/Cu + Laser + α PD-L1 group exhibited significantly elevated levels of both CD4⁺ T cells and CD8⁺ T cells in distant tumors (13.54% and 5.07%, respectively), in stark contrast to the baseline levels observed in the Saline-treated group (1.71% and 0.45%, respectively). For spleen, the levels of CD4⁺ T cells and CD8⁺ T cells in the Fc-SS-Fe/Cu + laser + α PD-L1 group (20.68% and 10.67%, respectively) are substantially higher than those in the Saline-treated group (6.18% and 2.02%, respectively). These promising findings validate the efficacy of Fc-SS-Fe/Cu combined PTT in stimulating anti-tumor immune responses, while also providing compelling evidence for the safety and efficacy of combined PD-L1-mediated ICB therapy as a viable strategy for cancer treatment.

3. Conclusion

In summary, we have developed a smart TME/NIR stimulus responsive nanoagent, Fc-SS-Fe/Cu, for efficient synergistic tumor therapy by ferroptosis, PTT and α PD-L1. Fc-SS-Fe/Cu rapidly disintegrated in response to TME, releasing bimetallic ions, ferrocene and disulfide bonds. The rapid consumption of GSH by Fe³⁺/Cu²⁺ and disulfide bonds further inhibited the expression of GPX4, while Fe²⁺/Cu⁺ and ferrocene initiated the Fenton/Fenton-like reactions that significantly augmented the intracellular ROS level and generate substantial amounts of LPO, thereby inducing ferroptosis. Simultaneously, ferroptosis effectively downregulates HSP70 expression, enhancing the mild-temperature PTT effect. Moreover, Fc-SS-Fe/Cu-induced ferroptosis/PTT can effectively trigger ICD, thereby addressing the issues of inadequate immunogenicity and insufficient immune infiltration. Importantly, the O₂-generating ability induced by Fc-SS-Fe/Cu effectively downregulates the expression of PD-L1 on tumor cell surfaces by inhibiting the HIF-1 α pathway, thereby augmenting the α PD-L1 therapeutic effect, which proves that Fc-SS-Fe/Cu is a potential nanomedicine that is well-suitable for PD-L1-mediated ICB therapy.

CRedit authorship contribution statement

Yujun Bao: Writing – review & editing, Writing – original draft, Methodology, Conceptualization. **Guanghao Li:** Investigation, Formal analysis, Data curation. **Siqi Li:** Project administration, Methodology, Investigation. **Haishui Zhou:** Validation, Supervision, Software. **Ziqing Yang:** Visualization, Software, Resources. **Zhiqiang Wang:** Visualization, Validation, Supervision. **Rui Yan:** Writing – original draft, Project administration, Funding acquisition. **Changhong Guo:** Writing – review & editing, Resources, Funding acquisition. **Yingxue Jin:** Writing – review & editing, Project administration, Funding acquisition.

Declaration of Competing Interest

The authors declare that they have no known competing financial interests or personal relationships that could have appeared to influence

the work reported in this paper.

Acknowledgements

Financial support for this research was provided by the Joint Foundation of Natural Science Foundation Heilongjiang Province of China (LH2020B010), and Graduate Innovation Projects of Harbin Normal University (HSDBSCX2024-09). The authors express gratitude to Fujing Guan (Harbin Center for Disease Control and Prevention) for her assistance during the experiment.

Appendix B. Supplementary data

Supplementary data to this article can be found online at <https://doi.org/10.1016/j.mtbio.2024.101346>.

Data availability

Data will be made available on request.

References

- [1] G. Chen, L. Lin, Z. Mai, Y. Tang, Q. Zhang, G. Chen, Z. Li, J. Zhang, Y. Wang, Y. Yang, Carrier-Free photodynamic bioregulators inhibiting lactic acid efflux combined with immune checkpoint blockade for triple-negative breast cancer immunotherapy, *ACS Nano* (2024), <https://doi.org/10.1021/acsnano.4c07213>.
- [2] Y. Dai, Z. Guo, D. Leng, G. Jiao, K. Chen, M. Fu, Y. Liu, Q. Shen, Q. Wang, L. Zhu, Metal-coordinated NIR-II nanoadducts with nanobody conjugation for potentiating immunotherapy by tumor metabolism reprogramming, *Adv. Sci.* (2024) 2404886, <https://doi.org/10.1002/adv.202404886>.
- [3] Q. Chen, H. Xiao, L. Hu, Y. Huang, Z. Cao, X. Shuai, Z. Su, 19F MRI/CEUS dual imaging-guided sonodynamic therapy enhances immune checkpoint blockade in triple-negative breast cancer, *Adv. Sci.* (2024) 2401182, <https://doi.org/10.1002/adv.202401182>.
- [4] J. Zhang, Y. Pan, L. Liu, Y. Xu, C. Zhao, W. Liu, L. Rao, Genetically edited cascade nanozymes for cancer immunotherapy, *ACS Nano* 18 (19) (2024) 12295–12310, <https://doi.org/10.1021/acsnano.4c01229>.
- [5] L. Fan, S. Qu, J. Qian, G. Shi, Q. Huang, Y. Song, Y. Ji, Q. Fan, X. Han, Melanin-based duplex Cas9 ribonucleoprotein nanomedicine for synergistic phototherapy and immunotherapy, *Chem. Eng. J.* (2024) 152754, <https://doi.org/10.1016/j.cej.2024.152754>.
- [6] Q. Zou, K. Liao, G. Li, X. Huang, Y. Zheng, G. Yang, M. Luo, E.Y. Xue, C. Lan, S. Wang, Photo-metallo-immunotherapy: fabricating chromium-based nanocomposites to enhance CAR-T cell infiltration and cytotoxicity against solid tumors, *Adv. Mater.* (2024) 2407425, <https://doi.org/10.1002/adma.202407425>.
- [7] M.-Y. Jung, B. Himes, L. Cumba-Garcia, I. Parney, INNV-32. SUPER-INDUCTION OF immunosuppressive glioblastoma extracellular vesicles BY IFN- γ , *Neuro Oncol.* 21 (Suppl 6) (2019) vi137, <https://doi.org/10.1093/neuonc/noz175.573>.
- [8] G. Chen, A.C. Huang, W. Zhang, G. Zhang, M. Wu, W. Xu, Z. Yu, J. Yang, B. Wang, H. Sun, Exosomal PD-L1 contributes to immunosuppression and is associated with anti-PD-1 response, *Nature* 560 (7718) (2018) 382–386, <https://doi.org/10.1038/s41586-018-0392-8>.
- [9] H. He, L. Xiao, J. Wang, D. Guo, Z. Lu, Aerobic glycolysis promotes tumor immune evasion and tumor cell stemness through the noncanonical function of hexokinase 2, *Cancer Commun.* 43 (3) (2023) 387, <https://doi.org/10.1002/cac2.12404>.
- [10] A. Nicolini, P. Ferrari, Involvement of tumor immune microenvironment metabolic reprogramming in colorectal cancer progression, immune escape, and response to immunotherapy, *Front. Immunol.* 15 (2024) 1353787, <https://doi.org/10.3389/fimmu.2024.1353787>.
- [11] X. Ding, L. Wang, X. Zhang, J. Xu, P. Li, H. Liang, X. Zhang, L. Xie, Z. Zhou, J. Yang, The relationship between expression of PD-L1 and HIF-1 α in glioma cells under hypoxia, *J. Hematol. Oncol.* 14 (1) (2021) 92, <https://doi.org/10.1186/s13045-021-01102-5>.
- [12] X. Zhang, C. He, X. He, S. Fan, B. Ding, Y. Lu, G. Xiang, HIF-1 inhibitor-based one-stone-two-birds strategy for enhanced cancer chemodynamic-immunotherapy, *J. Contr. Release* 356 (2023) 649–662, <https://doi.org/10.1016/j.jconrel.2023.03.026>.
- [13] P. Huang, Y. Yang, W. Wang, Z. Li, N. Gao, H. Chen, X. Zeng, Self-driven nanoprodug platform with enhanced ferroptosis for synergistic photothermal-Ido immunotherapy, *Biomaterials* 299 (2023) 122157, <https://doi.org/10.1016/j.biomaterials.2023.122157>.
- [14] H.N. Bell, B.R. Stockwell, W. Zou, Ironing out the role of ferroptosis in immunity, *Immunity* 57 (5) (2024) 941–956, <https://doi.org/10.1016/j.immuni.2024.03.019>.
- [15] A. Amos, A. Amos, L. Wu, H. Xia, The Warburg effect modulates DHODH role in ferroptosis: a review, *Cell Commun. Signal.* 21 (1) (2023) 100, <https://doi.org/10.1186/s12964-022-01025-9>.
- [16] M. Jaworska, J. Szczudło, A. Pietrzyk, J. Shah, S.E. Trojan, B. Ostrowska, K. A. Kocemba-Pilarczyk, The Warburg effect: a score for many instruments in the

- concert of cancer and cancer niche cells, *Pharmacol. Rep.* 75 (4) (2023) 876–890, <https://doi.org/10.1007/s43440-023-00504-1>.
- [17] W. Zhu, X. Cheng, P. Xu, Y. Gu, H. Xu, J. Xu, Y. Wang, L.W. Zhang, Y. Wang, Radiotherapy-Driven Nanoprobes Targeting for Visualizing Tumor Infiltration Dynamics and Inducing Ferroptosis in Myeloid-Derived Suppressor Cells, *J. Am. Chem. Soc.* (2024), <https://doi.org/10.1021/jacs.4c05650>.
- [18] H. Zhuang, L. Wang, S. Shao, H. Jing, P. Xue, T. Bai, J. Deng, X. Zeng, X. Qin, S. Yan, Photocatalysis-Promoted Tumor Ferroptosis Enabled by MOF-Derived Black TiO₂, *Chem. Eng. J.* (2024) 154204, <https://doi.org/10.1016/j.cej.2024.154204>.
- [19] Z. Liu, S. Liu, B. Liu, Q. Meng, M. Yuan, X. Ma, J. Wang, P.a. Ma, J. Lin, Tumor Microenvironment-Activatable Metal-Phenolic Nanoformulations for Ultrasound-Boosted Ferroptosis through Triple Regulatory Pathways, *Adv. Funct. Mater.* (2024) 2407153, <https://doi.org/10.1002/adfm.202407153>.
- [20] G. Gao, X. Sun, G. Liang, Nanoagent-Promoted Mild-Temperature Photothermal Therapy for Cancer Treatment, *Adv. Funct. Mater.* 31 (25) (2021) 2100738, <https://doi.org/10.1002/adfm.202100738>.
- [21] H. Hu, D. Li, W. Dai, Q. Jin, D. Wang, J. Ji, B.Z. Tang, Z. Tang, A NIR-II AIEgen-based Supramolecular Nanodot for Peroxynitrite-Potentiated Mild-Temperature Photothermal Therapy of Hepatocellular Carcinoma, *Adv. Funct. Mater.* 33 (19) (2023) 2213134, <https://doi.org/10.1002/adfm.202213134>.
- [22] M. Li, M. Hou, Q. Wu, Y. Jiang, G. Jia, X. Wu, C. Zhang, Simultaneous Inhibition of Heat Shock Response and Autophagy with Bimetallic Mesoporous Nanoparticles to Enhance Mild-Temperature Photothermal Therapy, *Small Struct.* 4 (11) (2023) 2300132, <https://doi.org/10.1002/sstr.202300132>.
- [23] K. Liu, L. Zhang, H. Lu, Y. Wen, B. Bi, G. Wang, Y. Jiang, L. Zeng, J. Zhao, Enhanced Mild-Temperature Photothermal Therapy by Pyroptosis-Boosted ATP Deprivation with Biodegradable Nanoformulation, *J. Nanobiotechnol.* 21 (1) (2023) 64, <https://doi.org/10.1186/s12951-023-01818-1>.
- [24] W. Cui, S. Zhu, X. Pan, W. Zhang, T. Wang, Gold (III) Porphyrin-Metal-Polyphenolic Nanocomplexes: Breaking Intracellular Redox Environment for Enhancing Mild-Temperature Photothermal Therapy, *ACS Appl. Mater. Interfaces* (2024), <https://doi.org/10.1021/acsami.4c04196>.
- [25] Y. Li, Y. Zhang, Y. Dong, O.U. Akakuru, X. Yao, J. Yi, X. Li, L. Wang, X. Lou, B. Zhu, Ablation of Gap Junction Protein Improves the Efficiency of Nanzyme-Mediated Catalytic/Starvation/Mild-Temperature Photothermal Therapy, *Adv. Mater.* 35 (22) (2023) 2210464, <https://doi.org/10.1002/adma.202210464>.
- [26] M. Chang, Z. Hou, M. Wang, C. Yang, R. Wang, F. Li, D. Liu, T. Peng, C. Li, J. Lin, Single-Atom Pd Nanzyme for Ferroptosis-Boosted Mild-Temperature Photothermal Therapy, *Angew. Chem., Int. Ed.* 60 (23) (2021) 12971–12979, <https://doi.org/10.1002/ange.202101924>.
- [27] W. Ying, Y. Zhang, W. Gao, X. Cai, G. Wang, X. Wu, L. Chen, Z. Meng, Y. Zheng, B. Hu, Hollow Magnetic Nanocatalysts Drive Starvation-Chemodynamic-Hyperthermia Synergistic Therapy for Tumor, *ACS Nano* 14 (8) (2020) 9662–9674, <https://doi.org/10.1021/acsnano.0c00910>.
- [28] G.-H. Chen, L. Gan, L.-Y. Tian, B.-X. Huang, Q. Xiao, Y.-J. Zhang, M.-T. Xiao, B.-D. Zheng, J. Ye, Mutually Reinforced Cancer Treatment Based on Phototherapy Combined with Ferroptosis, *Chem. Eng. J.* (2024) 152397, <https://doi.org/10.1016/j.cej.2024.152397>.
- [29] L. Chen, G. Chen, K. Hu, L. Chen, Z. Zeng, B. Li, G. Jiang, Y. Liu, Combined Photothermal and Photodynamic Therapy Enhances Ferroptosis to Prevent Cancer Recurrence after Surgery Using Nanoparticle-Hydrogel Composite, *Chem. Eng. J.* 468 (2023) 143685, <https://doi.org/10.1016/j.cej.2023.143685>.
- [30] T. Sun, L. Zhang, S. Xiao, Q. Xie, M. Wang, Y. Zhao, C. Zhou, M. Gong, D. Zhang, Activatable Plasmonic Versatile Nanoplatform for Glutathione-Depletion Augmented Ferroptosis and NIR-II Photothermal Synergistic Therapy, *ACS Mater. Lett.* 6 (3) (2024) 985–998, <https://doi.org/10.1021/acsmaterialslett.3c01533>.
- [31] H. Xiao, X. Li, S. Liang, S. Yang, S. Han, J. Huang, X. Shuai, J. Ren, Dual-Responsive Nanomedicine Activates Programmed Antitumor Immunity through Targeting Lymphatic System, *ACS Nano* 18 (17) (2024) 11070–11083, <https://doi.org/10.1021/acsnano.3c11464>.
- [32] D. Xu, Y. Li, S. Yin, F. Huang, Strategies to Address Key Challenges of Metallacycle/Metallacage-Based Supramolecular Coordination Complexes in Biomedical Applications, *Chem. Soc. Rev.* 53 (2024) 3167–3204, <https://doi.org/10.1039/d3cs00926b>.
- [33] Y. Ma, Y. Cao, M. Zu, Q. Gao, G. Liu, J. Ji, H. Xu, Q. Yang, X. Shi, R.L. Reis, Flying-saucer-shaped Nanoheterojunctions with Enhanced Colorectal Tumor Accumulation for Increased Oxidative Stress and Immunometabolic Regulation, *Adv. Funct. Mater.* (2024) 2402164, <https://doi.org/10.1002/adfm.202402164>.
- [34] X. Lin, F. Chen, X. Yu, H. Wang, H. Qiu, Y. Li, S. Yin, P.J. Stang, Phenylthiol-BODIPY-based Supramolecular Metallacycles for Synergistic Tumor Chemophotodynamic Therapy, *Proc. Natl. Acad. Sci. USA* 119 (29) (2022) e2203994119, <https://doi.org/10.1073/pnas.2203994119>.
- [35] Y. Liang, C. Peng, N. Su, Q. Li, S. Chen, D. Wu, B. Wu, Y. Gao, Z. Xu, Q. Dan, Tumor Microenvironments Self-Activated Cascade Catalytic Nanoscale Metal Organic Frameworks as Ferroptosis Inducer for Radiosensitization, *Chem. Eng. J.* 437 (2022) 135309, <https://doi.org/10.1016/j.cej.2022.135309>.
- [36] H. He, L. Du, H. Guo, Y. An, L. Lu, Y. Chen, Y. Wang, H. Zhong, J. Shen, J. Wu, Redox Responsive Metal Organic Framework Nanoparticles Induces Ferroptosis for Cancer Therapy, *Small* 16 (33) (2020) 2001251, <https://doi.org/10.1002/sml.202001251>.
- [37] S. Guo, Z. Li, R. Zhou, J. Feng, L. Huang, B. Ren, J. Zhu, Y. Huang, G. Wu, H. Cai, MRI-Guided Tumor Therapy Based on Synergy of Ferroptosis, Immunosuppression Reversal and Disulfidoptosis (2024) 2309842, <https://doi.org/10.1002/sml.202309842>. *Small*.
- [38] M. Zhang, Y. You, H. Zhang, J. Zhang, F. Yang, X. Wang, C. Lin, B. Wang, L. Chen, Z. Wang, Rapid Glutathione Analysis with SERS Microneedles for Deep Glioblastoma Tissue Differentiation, *Anal. Chem.* (2024), <https://doi.org/10.1021/acs.analchem.4c00483>.
- [39] Y. Yang, J. Xu, R. Zhou, Z. Qin, C. Liao, S. Shi, Y. Chen, Y. Guo, S. Zhang, Coordinated Carbon Dots-Fe Featuring Synergistically Enhanced Peroxidase-Like Activity at Neutral pH for Specific and Background-Free Detection of Dichlorvos, *Carbon* 219 (2024) 118831, <https://doi.org/10.1016/j.carbon.2024.118831>.
- [40] J. Xiao, F. Shi, Y. Zhang, M. Peng, J. Xu, J. Li, Z. Chen, Z. Yang, A MOF Nanzyme-Mediated Acetylcholinesterase-Free Colorimetric Strategy for Direct Detection of Organophosphorus Pesticides, *Chem. Commun.* 60 (8) (2024) 996–999, <https://doi.org/10.1039/d3cc05381d>.
- [41] A. Kumar, V.S. Goudar, B.K. Nahak, P.H. Tsai, H.W. Lin, F.G. Tseng, [Ru (dpp) 3] Cl₂-Embedded Oxygen Nano Polymeric Sensors: A Promising Tool for Monitoring Intracellular and Intratumoral Oxygen Gradients with High Quantum Yield and Long Lifetime, *Small* 20 (17) (2024) 2307955, <https://doi.org/10.1002/sml.202307955>.
- [42] Y. Liang, P. Lei, R. An, P. Du, S. Liu, Y. Wei, H. Zhang, Biodegradable Monometallic Aluminum as a Biotuner for Tumor Pyroptosis, *Angew. Chem., Int. Ed.* (2024) e20217304, <https://doi.org/10.1002/anie.202317304>.
- [43] P. Sun, L. Huang, Z. Li, Y. Yang, S. Lu, N. Gao, H. Chen, X. Zeng, Z. Xie, Charge-Reversal Biodegradable Nanoplatform with Ferroptosis and ICD Induction for Tumor Synergistic Treatment, *Chem. Eng. J.* (2024) 149234, <https://doi.org/10.1016/j.cej.2024.149234>.
- [44] J. Zhang, Y. Qin, Y. Chen, X. Zhao, J. Wang, Z. Wang, J. Li, J. Zhao, S. Liu, Z. Guo, Ultrathin 2D As₂Se₃ Nanosheets for Photothermal-Triggered Cancer Immunotherapy, *ACS Nano* (2024), <https://doi.org/10.1021/acsnano.3c10432>.
- [45] Y. Li, W. Fan, X. Gu, S. Liu, T. He, S. Gou, W. Meng, M. Li, X. Liu, Y. Ren, Biodegradable Ferric Phosphate Nanocarriers with Tumor-Specific Activation and Glutathione Depletion for Tumor Self-Enhanced Ferroptosis and Chemotherapy, *Adv. Funct. Mater.* (2024) 2313540, <https://doi.org/10.1002/adfm.202313540>.
- [46] D. Yu, Y. Wang, S. Qu, N. Zhang, K. Nie, J. Wang, Y. Huang, D. Sui, B. Yu, M. Qin, Controllable Star Cationic Poly (Disulfide)s Achieve Genetically Cascade Catalytic Therapy by Delivering Bifunctional Fusion Plasmids, *Adv. Mater.* 35 (52) (2023) 2307190, <https://doi.org/10.1002/adma.202307190>.
- [47] S. Liu, Y. Sun, J. Ye, C. Li, Q. Wang, M. Liu, Y. Cui, C. Wang, G. Jin, Y. Fu, Targeted Delivery of Active Sites by Oxygen Vacancy-Engineered Bimetal Silicate Nanozymes for Intratumoral Aggregation-Potentiated Catalytic Therapy, *ACS Nano* (2024), <https://doi.org/10.1021/acsnano.3c08780>.
- [48] Y. Liu, Y. Yi, S. Sun, T. Wang, J. Tang, Z. Peng, W. Huang, W. Zeng, M. Wu, Biodegradable and Efficient Charge-Migrated Z-Scheme Heterojunction Amplifies Cancer Ferroptosis by Blocking Defensive Redox System, *Small* (2023) 2309206, <https://doi.org/10.1002/sml.202309206>.
- [49] C. Wu, Z. Shen, Y. Lu, F. Sun, H. Shi, p53 Promotes Ferroptosis in Macrophages Treated with Fe₃O₄ Nanoparticles, *ACS Appl. Mater. Interfaces* 14 (38) (2022) 42791–42803, <https://doi.org/10.1021/acscami.2c00707>.
- [50] Z. Li, C. Wang, C. Dai, R. Hu, L. Ding, W. Peng, H. Huang, Y. Wang, J. Bai, Y. Chen, Engineering Dual Catalytic Nanomedicine for Autophagy-Augmented and Ferroptosis-Involved Cancer Nanotherapy, *Biomaterials* 287 (2022) 121668, <https://doi.org/10.1016/j.biomaterials.2022.121668>.
- [51] L. Huang, J. Zhu, W. Xiong, J. Feng, J. Yang, X. Lu, Y. Lu, Q. Zhang, P. Yi, Y. Feng, S. Guo, X. Qiu, Y. Xu, Z. Shen, Tumor-Generated Reactive Oxygen Species Storm for High-Performance Ferroptosis Therapy, *ACS Nano* 17 (12) (2023) 11492–11506, <https://doi.org/10.1021/acsnano.3c01369>.
- [52] T. Liao, Z. Chen, Y. Kuang, Z. Ren, W. Yu, W. Rao, L. Li, Y. Liu, Z. Xu, B. Jiang, Small-size Ti3C₂Tx MXene Nanosheets Coated with Metal-Polyphenol Nanodots for Enhanced Cancer Photothermal Therapy and Anti-Inflammation, *Acta Biomater.* 159 (2023) 312–323, <https://doi.org/10.1016/j.actbio.2023.01.049>.
- [53] X.-L. Ding, M.-D. Liu, Q. Cheng, W.-H. Guo, M.-T. Niu, Q.-X. Huang, X. Zeng, X.-Z. Zhang, Multifunctional Liquid Metal-Based Nanoparticles with Glycolysis and Mitochondrial Metabolism Inhibition for Tumor Photothermal Therapy, *Biomaterials* 281 (2022) 121369, <https://doi.org/10.1016/j.biomaterials.2022.121369>.
- [54] X. Shu, Y. Chen, P. Yan, Y. Xiang, Q.-Y. Shi, T. Yin, P. Wang, L.-H. Liu, X. Shuai, Biomimetic Nanoparticles for Effective Mild Temperature Photothermal Therapy and Multimodal Imaging, *J. Contr. Release* 347 (2022) 270–281, <https://doi.org/10.1016/j.jconrel.2022.05.010>.
- [55] W. Li, T. Ma, T. He, Y. Li, S. Yin, Cancer Cell Membrane-Encapsulated Biomimetic Nanoparticles for Tumor Immuno-Photothermal Therapy, *Chem. Eng. J.* 463 (2023) 142495, <https://doi.org/10.1016/j.cej.2023.142495>.
- [56] M. Lv, Y. Zheng, J. Wu, Z. Shen, B. Guo, G. Hu, Y. Huang, J. Zhao, Y. Qian, Z. Su, Evoking Ferroptosis by Synergistic Enhancement of a Cyclopentadienyl Iridium-Betulin Immune Agonist, *Angew. Chem., Int. Ed.* 135 (48) (2023) e202312897, <https://doi.org/10.1002/ange.202312897>.
- [57] C. Huang, X. Lin, T. Lin, W. Lin, Z. Gong, Q. Zheng, B. Li, H. Wang, Multifunctional Nanocomposites Induce Mitochondrial Dysfunction and Glucose Deprivation to Boost Immunogenic Ferroptosis for Cancer Therapy, *Chem. Eng. J.* 466 (2023) 143012, <https://doi.org/10.1016/j.cej.2023.143012>.
- [58] J. Liu, Q. You, S. Ye, J. Wang, R. Du, F. Liang, Z. He, C. Wang, L. Zhu, Y. Yang, T Lymphocyte-Derived Immunogenic Hybrid Nanovesicles for Immunosuppression Reversion and Boosted Photothermal Immunotherapy, *Nano Today* 55 (2024) 102148, <https://doi.org/10.1016/j.nantod.2024.102148>.
- [59] G. Zhang, X. Chen, X. Chen, K. Du, K. Ding, D. He, D. Ding, R. Hu, A. Qin, B. Z. Tang, Click-Reaction-Mediated Chemotherapy and Photothermal Therapy Synergistically Inhibit Breast Cancer in Mice, *ACS Nano* 17 (15) (2023) 14800–14813, <https://doi.org/10.1021/acsnano.3c03005>.

- [60] I.B. Barsoum, C.A. Smallwood, D.R. Siemens, C.H. Graham, A mechanism of hypoxia-mediated escape from adaptive immunity in cancer cells, *Cancer Res.* 74 (3) (2014) 665–674, <https://doi.org/10.1158/0008-5472.CAN-13-0992>.
- [61] C.M. Bailey, Y. Liu, M. Liu, X. Du, M. Devenport, P. Zheng, Y. Liu, Y. Wang, Targeting HIF-1 α abrogates PD-L1-mediated immune evasion in tumor microenvironment but promotes tolerance in normal tissues, *J. Clin. Invest.* 132 (9) (2022), <https://doi.org/10.1172/JCI150846>.
- [62] Y. Zhang, M.M. Rahman, P.A. Clark, R.N. Sriramaneni, T. Havighurst, C.P. Kerr, M. Zhu, J. Jones, X. Wang, K. Kim, In situ vaccination following intratumoral injection of IL2 and poly-L-lysine/iron oxide/CpG nanoparticles to a radiated tumor site, *ACS Nano* 17 (11) (2023) 10236–10251, <https://doi.org/10.1021/acsnano.3c00418>.
- [63] H.-H. Shen, J.-F. Peng, R.-R. Wang, P.-Y. Wang, J.-X. Zhang, H.-F. Sun, Y. Liang, Y.-M. Li, J.-N. Xue, Y.-J. Li, IL-12-Overexpressed nanoparticles suppress the proliferation of melanoma through inducing ICD and activating DC, CD8⁺ T, and CD4⁺ T cells, *Int. J. Nanomed.* (2024) 2755–2772, <https://doi.org/10.2147/ijn.s442446>.
- [64] T. Wang, M. Han, Y. Han, Z. Jiang, Q. Zheng, H. Zhang, Z. Li, Antigen self-presented personalized nanovaccines boost the immunotherapy of highly invasive and metastatic tumors, *ACS Nano* 18 (8) (2024) 6333–6347, <https://doi.org/10.1021/acsnano.3c11189>.
- [65] J. Ju, D. Xu, L. Xu, J. Liu, H. Zeng, B. Zhao, Y. Xiong, Y. Ma, G. Ge, H. Deng, Polysaccharide nanoadjuvants with precise drug composition for enhanced STING-mediated APC activation, *Eur. Polym. J.* (2024) 113333, <https://doi.org/10.1016/j.eurpolymj.2024.113333>.
- [66] D. Jorgovanovic, M. Song, L. Wang, Y. Zhang, Roles of IFN- γ in tumor progression and regression: a review, *Biomark. Res.* 8 (2020) 1–16, <https://doi.org/10.1186/s40364-020-00228-x>.
- [67] H. Zhang, Y. Cao, W. Li, S. Zhang, S. Song, Y. Wang, H. Zhang, Ferroptosis-induced immunomodulation with biometabolic MOF@ COF nanovaccine for self-boosting anti-tumor immunotherapy, *Chem. Eng. J.* (2024) 152675, <https://doi.org/10.1016/j.cej.2024.152675>.
- [68] Y. Lin, Y. Wang, Y. Peng, F. Liu, G. Lin, S. Huang, H. Sytwu, C. Cheng, Interleukin 26 skews macrophage polarization towards M1 phenotype by activating cJUN and the NF- κ B pathway, *Cells* 9 (4) (2020) 938, <https://doi.org/10.3390/cells9040938>.
- [69] C.A. Kraynak, D.J. Yan, L.J. Suggs, Modulating inflammatory macrophages with an apoptotic body-inspired nanoparticle, *Acta Biomater.* 108 (2020) 250–260, <https://doi.org/10.1016/j.actbio.2020.03.041>.
- [70] S. Kim, H.J. Chang, M.V. Volin, S. Umar, K.V. Raemdonck, A. Chevalier, K. Palasiewicz, J.W. Christman, S. Volkov, S. Arami, M. Maz, A. Mehta, R. K. Zomorrodi, D.A. Fox, N. Sweiss, S. Shahrara, Macrophages are the primary effector cells in IL-7-induced arthritis, *Cell. Mol. Immunol.* 17 (2020) 728–740, <https://doi.org/10.1038/s41423-019-0235-z>.